RSC Advances

PAPER

View Article Online
View Journal | View Issue

Cite this: *RSC Adv.*, 2024, **14**, 11734

Rational synthesis of 3D coral-like $ZnCo_2O_4$ nanoclusters with abundant oxygen vacancies for high-performance supercapacitors†

Yanlei Bi,[a] Huiqing Fan, *[a] Chuansen Hu,[a] Ru Wang,[a] Lujie Niu,[a] Guangwu Wen[b] and Luchang Qin[c]

Transition metal oxides with high theoretical capacitance are regarded as desired electrode materials for supercapacitors, however, the poor conductivity and sluggish charge transfer kinetics constrain their electrochemical performance. The three-dimensional (3D) coral-like $ZnCo_2O_4$ nanomaterials with abundant oxygen vacancies were synthesized through a facile hydrothermal method and chemical reduction approach. The introduced oxygen vacancies can provide more active sites and lower the energy barrier, thereby facilitating the kinetics of surface reactions. Furthermore, the abundant oxygen vacancies in metal oxides can function as shallow donors to facilitate charge carrier diffusion, resulting in a faster ion diffusion rate and superior electrochemical conductivity. The electrochemical performance of $ZnCo_2O_4$ was optimized by the introduction of oxygen vacancies. The $ZnCo_2O_4$ nanoclusters, reduced by 0.5 M $NaBH_4$ ($ZnCo_2O_4$-0.5), exhibit a specific capacitance of 2685.7 F g^{-1} at 1 A g^{-1}, which is nearly twice that of the pristine $ZnCo_2O_4$ (1525.7 F g^{-1} at 1 A g^{-1}). The $ZnCo_2O_4$-0.5 exhibits an excellent rate capacity (81.9% capacitance retention at 10 A g^{-1}) and a long cycling stability (72.6% specific capacitance retention after 10 000 cycles at 3 A g^{-1}). Furthermore, the asymmetric supercapacitor (ASC, $ZnCo_2O_4$-0.5 nanoclusters//active carbon) delivers a maximum energy density of 50.2 W h kg^{-1} at the power density of 493.7 W kg^{-1} and an excellent cycling stability (75.3% capacitance retention after 3000 cycles at 2 A g^{-1}), surpassing the majority of previously reported $ZnCo_2O_4$-based supercapacitors. This work is important for revealing the pivotal role of implementing the defect engineering regulation strategy in achieving optimization of both electrochemical activity and conductivity.

Received 5th February 2024
Accepted 2nd April 2024

DOI: 10.1039/d4ra00927d

rsc.li/rsc-advances

1. Introduction

With the growing ubiquity of unmanned intelligent systems and portable wearable devices, contemporary society necessitates an ever-increasing amount of energy.[1] To mitigate the prevailing energy scarcity, extensive research is being conducted on energy storage devices that exhibit remarkable attributes such as substantial capacity and fast-charging abilities.[2] Compared to lithium-ion batteries, which are costly and pose safety concerns due to the formation of lithium dendrites during charging and discharging processes,[3] supercapacitors (SCs) emerge as ideal candidates for electrochemical energy storage devices owing to their exceptional power density, rapid recharge capabilities, prolonged lifespan, and environmental friendliness.[4] Nevertheless, the limited energy density of SCs significantly hinders their practical utilization.[5] The objective is to facilitate the commercialization of SCs; considerable attempts have pursued exploration of electrode materials possessing high theoretical capacity and electrochemical activity.[6]

Up to now, the spinel cobalt-based oxide has garnered significant attention in the realm of electrode materials research.[7] In comparison to simple monometallic oxides,[8] various ternary metal oxides (*e.g.*, $ZnCo_2O_4$,[9] $NiCo_2O_4$,[10] and $CuCo_2O_4$ (ref. 11)) possess notable advantages, including high theoretical capacitance, multiple oxidation states, and abundant reserves on Earth, thereby exhibiting outstanding electrochemical properties.[12] However, the poor intrinsic conductivity and sluggish charge transfer kinetics of $ZnCo_2O_4$ significantly compromise its specific capacitance,[13] which falls far below the theoretical value and fails to meet expectations. Extensive research has been implemented to overcome these bottlenecks, including the design of 3D structures and composites with high electrical conductivity materials (*e.g.*, MXenes[14] and graphene[11]). Li *et al.* synthesized the hierarchical cactus-like $ZnCo_2O_4$ films on nickel foam (NF) *via* 3D structure design,

[a]School of Chemistry and Chemical Engineering, Shandong University of Technology, Zibo 255000, China. E-mail: huiqingfan@yeah.net; hqfan@sdut.edu.cn
[b]School of Materials Science and Engineering, Shandong University of Technology, Zibo 255000, China
[c]Department of Physics and Astronomy, University of North Carolina at Chapel Hill, Chapel Hill, NC 27599-3255, USA

† Electronic supplementary information (ESI) available. See DOI: https://doi.org/10.1039/d4ra00927d

thereby increasing the electrode/electrolyte interface area and demonstrating an exceptionally high specific capacity of 1115.7 F g^{-1} at a current density of 1 A g^{-1}.[15] The investigation conducted by Bhagwan *et al.* focused on reducing the electron/ion diffusion length of $ZnCo_2O_4$ nanoparticles through nanostructure engineering, which exhibited a specific capacitance of 843 F g^{-1} at 1 A g^{-1} and experienced only an 8.5% capacity loss after undergoing 2000 cycles.[16] Nevertheless, the existing strategies can only enhance the electrochemical performance of $ZnCo_2O_4$ materials to a certain extent without altering their inherent properties,[17] the research on SCs has yet to meet the anticipated advancements.

Defect engineering of electrode materials has emerged as a highly effective strategy in the realm of electrochemical energy storage.[18] Numerous studies have proved that the defect energy level could induce impurity states in the bandgap and serve as shallow donors to increase the concentration of carriers, thereby enhancing the intrinsic conductivity of electrode materials.[19] Incorporating oxygen vacancies into metal oxides can disrupt the metal–oxygen bonds and intrinsically change the electronic structure of metallic oxides, leading to an increased number of delocalized electrons and enhanced charge transport capacity. Furthermore, oxygen vacancies can function as electroactive sites,[20] reducing the activation energy of pseudocapacitive reactions, accelerating surface redox reactions, and greatly boosting electrochemical performance.[21] Liu *et al.* successfully synthesized the long-range disordered MoO_2 with rich oxygen vacancies, exhibiting an impressive specific capacity of 1631.3 mA h g^{-1} at a current density of 0.2 A g^{-1} and demonstrating excellent rate capability (592.6 mA h g^{-1} at 8.0 A g^{-1}).[22]

The strategies for inducing oxygen vacancies primarily revolve around hydrogen treatment,[23] post-annealing in oxygen-deficient atmospheres,[24] ion doping,[25] or electron irradiation.[26] However, the aforementioned strategies often exhibit drawbacks such as high risks of hydrogen explosion, elevated temperature conditions, low efficiency, and intricate experimental procedures, thereby impeding the implementation of introducing oxygen vacancies in transition metal oxides. Compared to the above strategies, chemical reduction is a straightforward method with a gentle and controllable reaction process. The relative content of oxygen vacancies can be effectively modulated by manipulating the reaction temperature, duration, and reducing agent dosage.[27,28] The utilization of $NaBH_4$ as a reducing agent for the chemical reduction method has garnered significant attention in introducing oxygen vacancies in transition metal oxides. Under the influence of $NaBH_4$ aqueous solution, the reducing molecule initially adsorbs onto the surface of the metal oxide, facilitating the reduction of partial metal ions within the oxide to a lower oxidation state.[29] Subsequently, electron transfer enables the capture of an oxygen atom from surface oxygen,[30] resulting in the formation of oxygen vacancies. The process of $NaBH_4$ reduction is governed by the following mechanism:[31,32]

$$MO + \frac{x}{8}NaBH_4 + \frac{x}{4}H_2O = MO_{1-x}(OH)_x + \frac{x}{8}NaBO_2 \quad (1)$$

Unfortunately, there are rare reports involving the application of defect engineering and structure design to $ZnCo_2O_4$ materials. Therefore, developing facile and efficient strategies for the introduction of oxygen vacancies into 3D $ZnCo_2O_4$ electrode materials is still an ideal strategy for achieving enhanced electrochemical performance.

Herein, the novel coral-like $ZnCo_2O_4$-0.5 nanoclusters were synthesized utilizing a straightforward and secure methodology. The $ZnCo_2O_4$ nanoclusters firmly adhere to the NF substrate through a one-step hydrothermal process followed by a subsequent calcination step, eliminating the need for conductive agents and binders. Afterwards, $NaBH_4$ was utilized as a reducing agent for obtaining the final product. In addition, by optimizing the concentration of $NaBH_4$ and fine-tuning the reduction time, the resulting electrode material exhibits higher conductivity, multiple active sites, and remarkable mechanical robustness. Furthermore, the introduction of oxygen vacancies into $ZnCo_2O_4$ is successfully achieved through this simple and efficient method, while preserving its original morphology and structure to the greatest extent. Benefiting from the aforementioned profitable properties, the resultant coral-like $ZnCo_2O_4$-0.5 nanoclusters exhibit a specific capacitance of 2685.7 F g^{-1} at a current density of 1 A g^{-1}, representing an approximately twofold increase compared to that of the untreated $ZnCo_2O_4$. Moreover, the assembled ASC device of $ZnCo_2O_4$-0.5 nanoclusters//active carbon (AC) delivers a superb energy density of 50.2 W h kg^{-1} at a power density of 493.7 W kg^{-1} and shows satisfactory cycling performance (75.32% capacitance retention after 3000 cycles at 2 A g^{-1}).

2. Experimental section

2.1. Chemicals

The reagents used in this research are of analytical grade. Sinopharm Chemical Reagent supplied zinc sulfate heptahydrate ($ZnSO_4 \cdot 7H_2O$, ≥99.5%), cobalt sulfate heptahydrate ($CoSO_4 \cdot 7H_2O$, ≥98.5%), ammonium fluoride (NH_4F, ≥96.0%) and urea (CH_4N_2O, ≥98.5%). The experiments were conducted using deionized water.

2.2. Synthesis of pristine $ZnCo_2O_4$ and $ZnCo_2O_4$ with abundant oxygen vacancies (OV-$ZnCo_2O_4$)

The Ni foam (NF) underwent sequential pretreatment with acetone and dilute hydrochloric acid initially, followed by multiple rinses using deionized (DI) water and ethanol. Afterward, it was dried at 60 °C for 12 hours to obtain the pristine NF substrate.

In a typical preparation of the $ZnCo_2O_4$, 6 mmol $ZnSO_4 \cdot 7H_2O$, 12 mmol $CoSO_4 \cdot 7H_2O$, 36 mmol NH_4F, and 90 mmol CH_4N_2O in 200 mL DI water were mixed to obtain a homogeneous solution. The obtained mixture was stirred for 15 minutes to yield a transparent pink solution, which was subsequently transferred into a 50 mL Teflon-lined stainless steel autoclave. And then the NF substrate (effective reaction surface area: 1 × 2 cm^2) was immersed in the reactant solution contained within the Teflon-lined vessel. The autoclave was

subsequently placed in a blast oven and subjected to heating at 120 °C for 5 hours. Following cooling of the autoclave to ambient temperature, the substrate containing the precursor underwent sequential rinsing with deionized water and anhydrous ethanol. The precursor was ultimately subjected to calcination at 300 °C for 3 hours in the air using a muffle furnace with a heating rate of 2 °C min^{-1}, resulting in the formation of the $ZnCo_2O_4$ material. The NF coated with $ZnCo_2O_4$ was immersed in $NaBH_4$ solutions of varying concentrations (0.3 M, 0.5 M, 0.8 M, and 1 M) for 20 minutes, followed by rinsing with DI water and ethanol, subsequently dried at 60 °C for 12 hours under vacuum. The final products were named $ZnCo_2O_4$-0.3, $ZnCo_2O_4$-0.5, $ZnCo_2O_4$-0.8, and $ZnCo_2O_4$-1.0, respectively. The areal mass loading of active materials on Ni foam substrate was ~1.08 mg cm^{-2}. In addition, Table S1† shows the weight variations of Ni foam after different treatments during the experiment.

2.3. Material characterization

The crystal structure was analyzed by X-ray powder diffraction (XRD Rigaku, Japan, D/max-2200PC diffractometer with Cu Kα). Field emission scanning electron microscope (SEM, Gemini 300-71-31) and high-resolution electron microscope (TEM, FEI Talos F200x) were utilized to investigate the morphology and compositions of the as-synthesized materials. The chemical composition and surface electronic states were characterized by XPS (with an X-ray source of Thermo Scientific K-Alpha America). The Bruker EMXplus-6/1 EPR spectrometer detected the EPR signal. The specific surface area and the corresponding pore size distribution were evaluated by Brunauer–Emmett–Teller (BET, NOVA 4000e).

2.4. Electrochemical characterization

To investigate the impact of oxygen vacancies introduction on electrochemical performance, the as-prepared $ZnCo_2O_4$ and OV-$ZnCo_2O_4$ samples were analyzed using an electrochemical workstation (CHI 660E, Chenhua, China) by a three-electrode system in 6 M KOH electrolyte. The as-prepared electroactive materials were employed directly as the working electrode, and an Ag/AgCl electrode and a platinum foil were utilized as the reference electrode and counter electrode, respectively. Cyclic voltammetry (CV), galvanostatic charging-discharging (GCD), and electrochemical impedance spectroscopy (EIS) were carried out at room temperature to test electrochemical properties. The specific capacitance (C_{sp}) of the as-prepared electrode was calculated by the following equation:

$$C_{sp} = \frac{I \times \Delta t}{m \times \Delta V} \quad (2)$$

where I (A) is the constant discharge current, Δt (s) is the discharge time, ΔV (V) is the discharge potential window, and m (g) is the mass of the active material.

2.5. Fabrication of $ZnCo_2O_4$-0.5//AC ASC device

An ASC device was assembled using the as-prepared $ZnCo_2O_4$-0.5 materials as the positive electrode, AC as the negative electrode, and aqueous 6 M KOH as the electrolyte. Moreover, the balance of charges ($q^+ = q^-$) was considered to determine the most optimal mass ratio for the positive and negative electrodes as follows:

$$\frac{m^+}{m^-} = \frac{C^- \times \Delta V^-}{C^+ \times \Delta V^+} \quad (3)$$

where m (g), C (F g^{-1}), and ΔV (V) represent the mass, specific capacitance, and voltage range of positive and negative electrodes, respectively.

The energy density (E, W h kg^{-1}) and power density (P, W kg^{-1}) can be calculated by the following equation:

$$E = \frac{1}{2} C_{sp} \times \Delta V^2 \quad (4)$$

$$P = \frac{E}{\Delta t} \quad (5)$$

where C_{sp} (F g^{-1}) is the specific capacitance, Δt (s) is the discharge time, ΔV (V) is the discharge potential window.

3. Results and discussion

The synthetic process of the 3D coral-like $ZnCo_2O_4$-0.5 nanoclusters with abundant oxygen vacancies is shown in Scheme 1. Firstly, hydrothermal and calcination processes are carried out to facilitate the growth of $ZnCo_2O_4$ on the NF skeleton. Afterwards, the pristine $ZnCo_2O_4$ are immersed in $NaBH_4$ solutions with varying concentrations (0.3 M, 0.5 M, 0.8 M, and 1.0 M) and the resulting products are subsequently dried at 60 °C for 12 hours under vacuum.

To examine the impact of introducing oxygen vacancies on the crystalline structure, the X-ray diffraction (XRD) patterns of $ZnCo_2O_4$ and OV-$ZnCo_2O_4$ (with different $NaBH_4$ concentrations) were shown in Fig. 1a, the same diffraction peaks of all samples situated at 19.0°, 31.2°, 36.8°, 59.3°, and 65.2° are exclusively indexed to the (111), (220), (311), (511), and (440) planes of cubic $ZnCo_2O_4$ phase (JCPDS card No. 23-1390).[33] The aforementioned results indicate that the crystal structure has no obvious change during the $NaBH_4$ reduction process.[34] The XRD patterns were analyzed with correlational Rietveld refinement to characterize the structure of the synthesized materials (Fig. S1–S2 and Table S2†). Compared with that of pristine $ZnCo_2O_4$, the crystallinity of the $ZnCo_2O_4$-0.5 decreased. The Zn : Co : O ratio of $ZnCo_2O_4$ and $ZnCo_2O_4$-0.5 is 1 : 2 : 3.90 and 1 : 2 : 3.66, respectively, indicating that the formation of oxygen vacancies in $ZnCo_2O_4$-0.5 material.[24,35,36]

The structures and morphologies of pristine $ZnCo_2O_4$ and $ZnCo_2O_4$-0.5 are investigated by SEM images. Fig. 1b and c depict SEM images of pristine $ZnCo_2O_4$, the nanowires have uniform growth on the surface of NF substrate with an average width of approximately 15 nm and length of 2 μm. Fig. 1d–f present SEM images of $ZnCo_2O_4$-0.5 samples. After the reduction treatment, it can be observed in Fig. 1d that the $ZnCo_2O_4$-0.5 nanowires uniformly adhered to the NF substrate. Fig. 1e indicates the morphology of $ZnCo_2O_4$-0.5, remains largely consistent with that of the pristine $ZnCo_2O_4$, the nanowires intersect with each other, resulting in the formation of 3D coral-

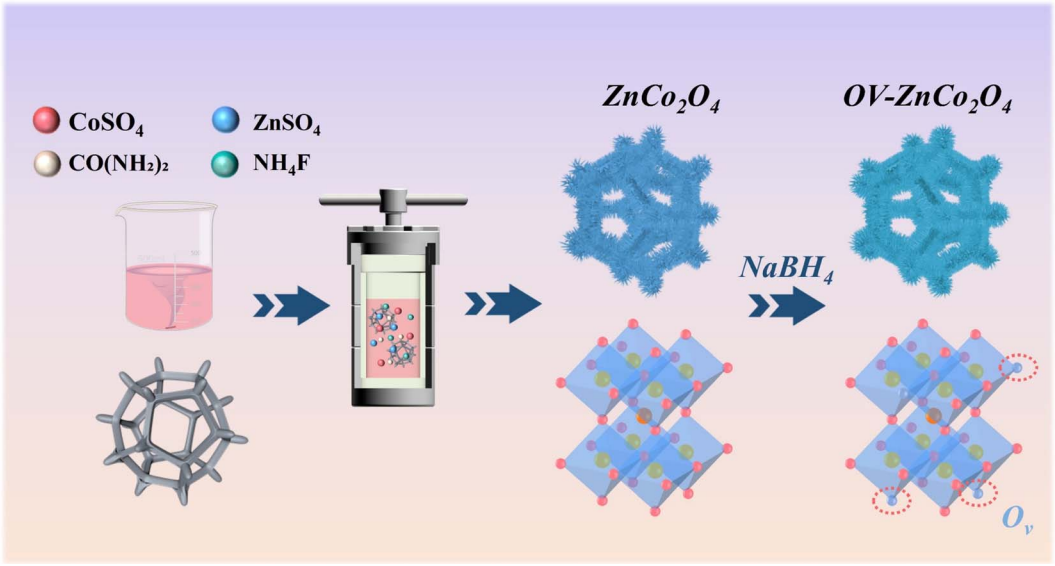

Scheme 1 The synthetic illustration of pristine $ZnCo_2O_4$ and $ZnCo_2O_4$-0.5 nanoclusters.

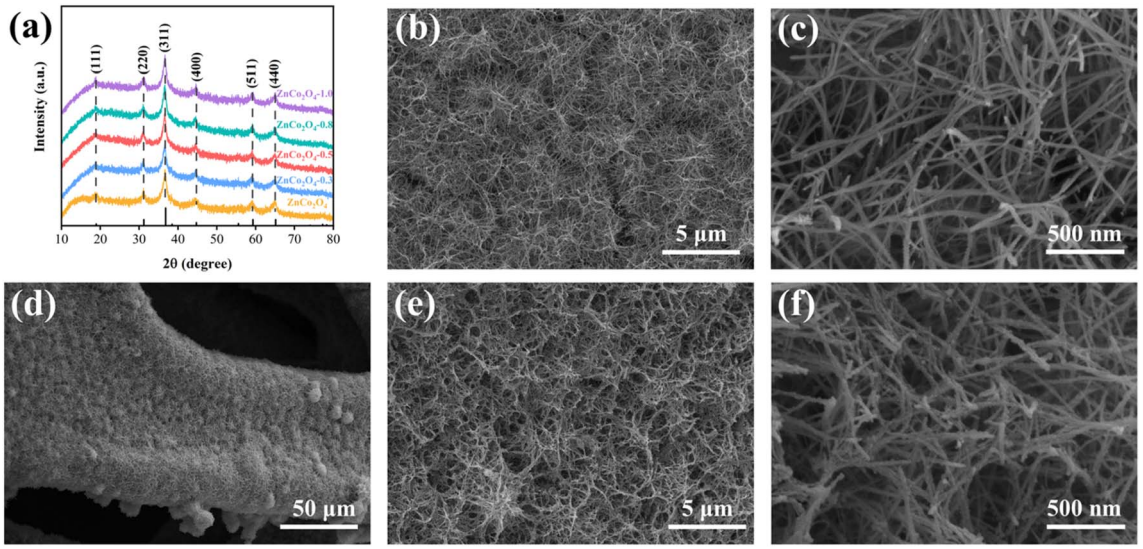

Fig. 1 (a) XRD patterns of $ZnCo_2O_4$ and OV-$ZnCo_2O_4$ (with different $NaBH_4$ concentrations). (b and c) SEM images of pristine $ZnCo_2O_4$ nanoclusters on NF. (d–f) SEM images of $ZnCo_2O_4$-0.5 nanoclusters on NF.

like $ZnCo_2O_4$-0.5 nanoclusters. Additionally, the surface of nanowires shows an increased roughness after undergoing reduction treatment (Fig. 1f). The 3D coral-like $ZnCo_2O_4$-0.5 nanoclusters with rougher surface not only enhance the material's surface area and facilitate electrode–electrolyte contact but also provide additional active sites, thereby accelerating the redox reaction rate and optimizing its electrochemical performance.[37] Additionally, SEM images of OV-$ZnCo_2O_4$ materials obtained with varying concentrations of $NaBH_4$ solution are presented in Fig. S3,† the morphology of nanoclusters is preserved after reduction by 0.3 M $NaBH_4$ in $ZnCo_2O_4$-0.3. When the concentration was increased to 0.8 M or 1 M, $ZnCo_2O_4$-0.8 and $ZnCo_2O_4$-1.0 could still partially maintain the original structure. However, due to its limited mechanical adhesion, the active material detaches from the NF substrate and compromises the integrity of the electrode structure, consequently leading to a reduction in electrochemical capacity.

The microstructure of $ZnCo_2O_4$-0.5 was further evidenced through TEM images. Fig. 2a provides further support for the 3D coral-like $ZnCo_2O_4$-0.5 nanoclusters are composed of interwoven nanowires. As shown in the HRTEM image (Fig. 2b), the well-defined lattice fringes of 0.241 nm, 0.278 nm, and 0.459 nm are assigned to the (111), (220), and (311) planes of the cubic $ZnCo_2O_4$ phase, respectively.[38] As shown in Fig. 2c, the selected area electron diffraction (SAED) pattern also follows the XRD

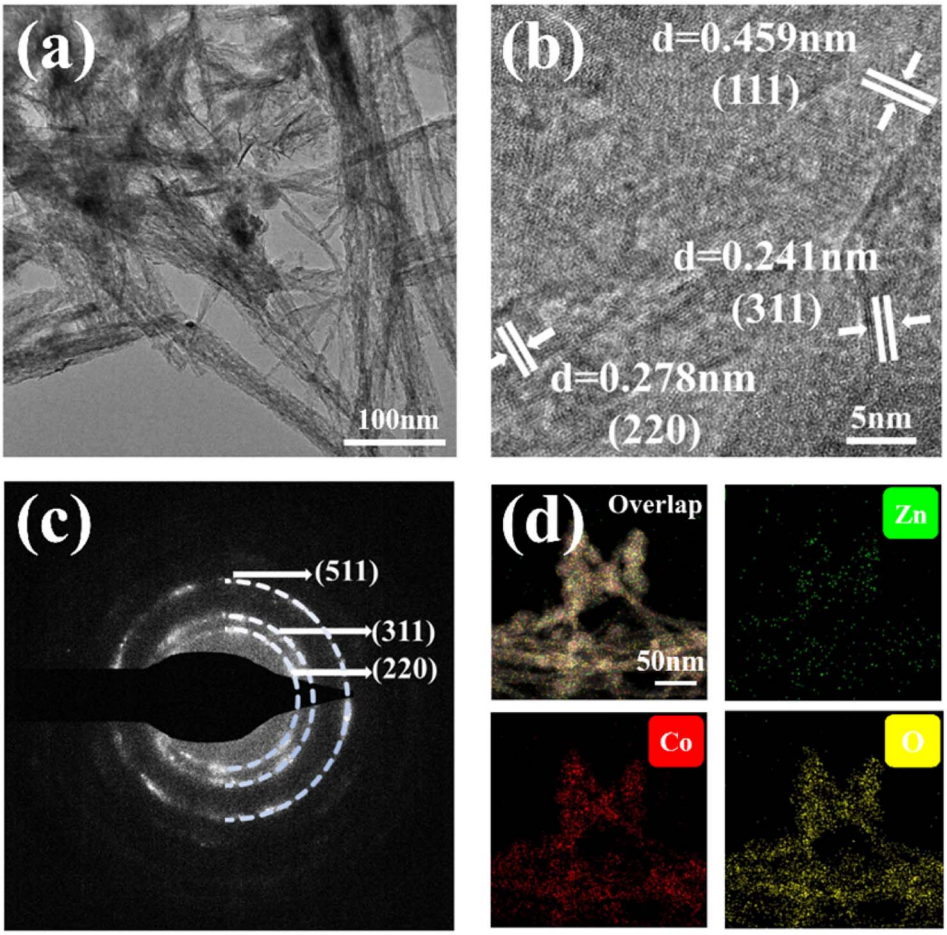

Fig. 2 (a) TEM image of $ZnCo_2O_4$-0.5 nanoclusters. (b) HRTEM image, (c) SAED image, and (d) TEM elemental mapping analysis image of $ZnCo_2O_4$-0.5 nanoclusters.

results, several diffraction rings can be indexed to the (220), (311), and (511) facets of the spinel $ZnCo_2O_4$ phase.[39] The STEM image and energy dispersive spectroscopy (EDS) mapping characterization in Fig. 2d demonstrate a homogeneous distribution of Co, Zn, and O throughout the representative $ZnCo_2O_4$-0.5.

The specific surface area and pore size distribution were investigated through the analysis of N_2 adsorption–desorption isotherms. As shown in Fig. S4a,† both pristine $ZnCo_2O_4$ and $ZnCo_2O_4$-0.5 display a characteristic IV isotherm with an H_3-type hysteresis loop, indicating their mesoporous properties.[40] The specific surface area of $ZnCo_2O_4$ and $ZnCo_2O_4$-0.5 were calculated by the BET method, revealing that the latter exhibited a significantly higher specific surface area (116.1 $m^2\ g^{-1}$) compared to pristine $ZnCo_2O_4$ (99.1 $m^2\ g^{-1}$). Moreover, the pore size distribution was depicted in Fig. S4b,† it has been determined that the average pore diameter of $ZnCo_2O_4$-0.5 (10.1 nm) surpasses that of $ZnCo_2O_4$ (8.7 nm). The larger specific surface area and mesoporous structure of $ZnCo_2O_4$-0.5 provide more active sites for redox reactions and enhance the penetration of electrolyte into the electrode materials.[41]

To reveal the surface chemical composition and electronic states of the pristine $ZnCo_2O_4$ and $ZnCo_2O_4$-0.5 nanoclusters, the XPS analysis was conducted. The wide-scan XPS spectra in Fig. 3a confirm the existence of Zn, Co, O, and Ni in both of them. The Ni component was derived from the NF substrate and the C 1s was used to rectify the binding energy.[42] The Co 2p XPS spectra are presented in Fig. 3b. The two prominent peaks for pristine $ZnCo_2O_4$ were located at 780.1 eV and 794.9 eV, while that of $ZnCo_2O_4$-0.5 at 780.8 and 796.1 eV, which corresponded to the Co $2p_{3/2}$ and Co $2p_{1/2}$ spin–orbit components, respectively.[43] The fitted results indicate that the distinct peaks for $ZnCo_2O_4$ at 779.8 and 794.8 eV were attributed to Co^{3+}, while the peaks at 781.8 and 796.8 eV correspond to Co^{2+}. With regard to the $ZnCo_2O_4$-0.5, the binding energies located at 779.9 and 796.1 eV are corresponded to Co^{3+}, and at 781.8 and 798.1 eV are associated with Co^{2+}, the Co 2p spectrum exhibits a slight blue shift which further indicates the reduction reaction.[44] The intensities of the Co^{2+} peaks increased for $ZnCo_2O_4$-0.5 in comparison with that of pristine $ZnCo_2O_4$, accompanied by a decrease in the Co^{3+} peaks. This observation indicates that the reduction treatment promotes the conversion of high-valence Co^{3+} cations to lower-valence Co^{2+} cations while also promoting the generation of oxygen vacancies.[45] By quantifying the peak area percentage of $ZnCo_2O_4$ and $ZnCo_2O_4$-0.5, the atomic ratio of Co^{2+}/Co^{3+} on the surface changes from 0.54 to

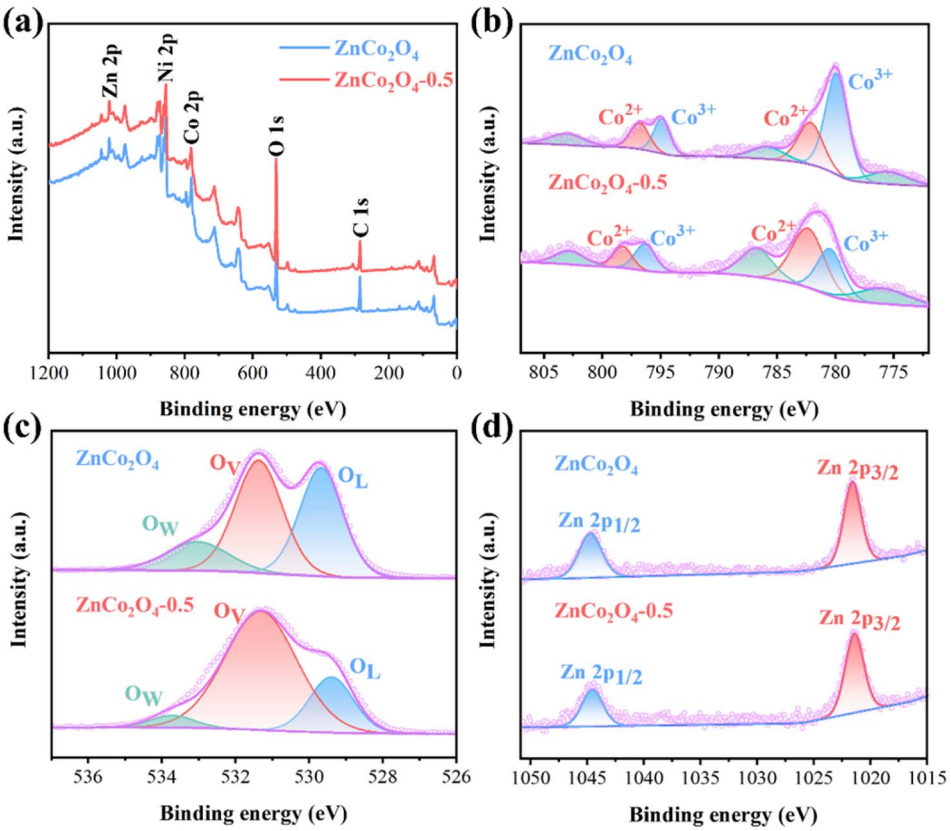

Fig. 3 XPS spectra of pristine $ZnCo_2O_4$ and $ZnCo_2O_4$-0.5 nanoclusters: (a) wide-scan, (b) Co 2p, (c) O 1s and (d) Zn 2p.

1.22, which further indicates the partial reduction of Co^{3+} to Co^{2+}. Moreover, the observed satellite peaks for both $ZnCo_2O_4$ and $ZnCo_2O_4$-0.5 detected at 775.6, 786.2, and 802.7 eV exhibit specific characteristics associated with Co^{2+}, the introduction of oxygen vacancies leads to the conversion of Co^{3+} into Co^{2+}, resulting in more intense satellite peaks for the $ZnCo_2O_4$-0.5.[36] As for the O 1s high-resolution level spectra (Fig. 3c), three characteristic peaks for pristine $ZnCo_2O_4$ were located at 529.6, 531.4, and 533.1 eV, while that of $ZnCo_2O_4$-0.5 at 529.3, 531.4, and 533.8 eV, which attributed to the presence of the lattice oxygen (O_L), oxygen vacancy (O_V), and physico- and chemisorbed water (O_W), respectively.[46] After the $NaBH_4$ treatment, the intensity of the lattice oxygen bond peak weakened, while there was an increase in the intensity of the oxygen vacancy peak. Based on the percentage of O_V peaks area of $ZnCo_2O_4$ and $ZnCo_2O_4$-0.5, the proportion of O_V increases from 44.8% to 73.6%, which further confirms the increase in oxygen vacancy content. As shown in Fig. 3d, two types of zinc species (Zn $2p_{3/2}$ and Zn $2p_{1/2}$) are observed, with characteristic spin–orbit peaks at 1021.7 and 1044.8 eV corresponding to each type respectively.[47] The spectra indicate the presence of Zn(II) oxidation state for pristine $ZnCo_2O_4$ and $ZnCo_2O_4$-0.5. Therefore, based on XPS analysis, a significant alteration in the electron valence state of $ZnCo_2O_4$ is observed after reduction treatment, which supports the idea that the increased concentration of oxygen vacancies enhances the electrochemical performance of supercapacitors.[48]

To provide additional evidence for the existence of oxygen vacancies, the electron paramagnetic resonance (EPR) spectra are performed in Fig. S5.† The spectra of $ZnCo_2O_4$ and $ZnCo_2O_4$-0.5 samples exhibit a symmetrical EPR signal at $g \sim 2.000$ and $g \sim 2.002$, respectively, which can be explained by the electron trapped in the oxygen vacancy.[49] The $ZnCo_2O_4$-0.5 has a higher intensity of EPR signal than pristine $ZnCo_2O_4$, revealing that the $NaBH_4$ reduction treatment instigates the formation of rich oxygen vacancies. Based on the analysis of the EPR signal, the oxygen vacancy concentrations of $ZnCo_2O_4$ and $ZnCo_2O_4$-0.5 are calculated to be 2.823×10^{11} spins per mm^3 and 4.580×10^{11} spins per mm^3, respectively. The results demonstrated the successful introduction of oxygen vacancies following the reduction treatment, thereby substantiating the XPS-based conclusion.[35]

To investigate the impact of oxygen vacancies introduction on electrochemical performance, a three-electrode device was fabricated using $ZnCo_2O_4$ and $ZnCo_2O_4$-0.5 as working electrodes, while a 6 M KOH aqueous solution was employed as the electrolyte.

Fig. 4a shows CV curves at a scan rate of 50 mV s^{-1}. Both $ZnCo_2O_4$ and $ZnCo_2O_4$-0.5 can observe a pair of well-defined redox peaks, which are indicative of the characteristic pseudocapacitance behavior exhibited by electrode materials.[50] The above redox reactions are mainly based on the following Faraday redox reactions:[16,51,52]

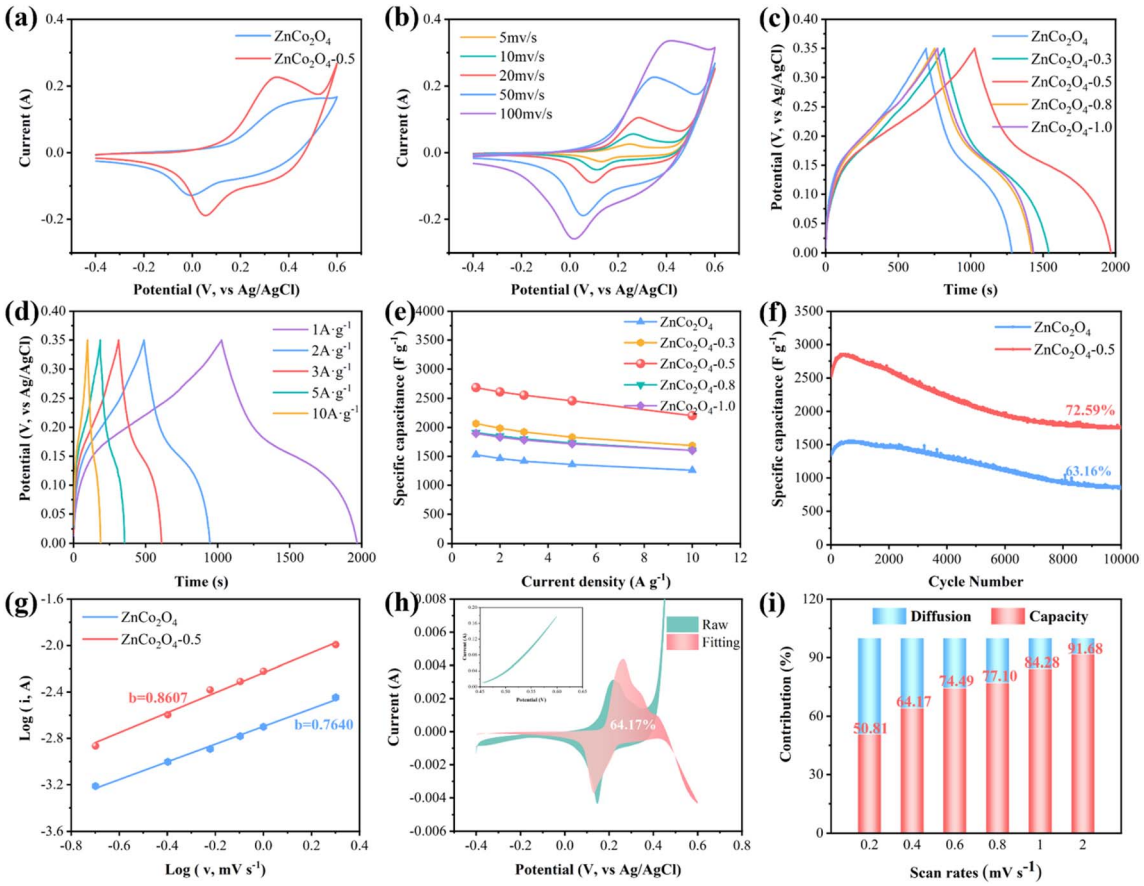

Fig. 4 (a) CV curves of $ZnCo_2O_4$ and $ZnCo_2O_4$-0.5 nanoclusters at the scan rate of 50 mV s^{-1}. (b) CV curves at different scan rates of $ZnCo_2O_4$-0.5 nanoclusters. (c) GCD curves of $ZnCo_2O_4$ and OV-$ZnCo_2O_4$ (with different $NaBH_4$ concentrations) at the current density of 1 A g^{-1}. (d) GCD curves at different current densities of $ZnCo_2O_4$-0.5 nanoclusters. (e) Specific capacitances of $ZnCo_2O_4$ and OV-$ZnCo_2O_4$ (with different $NaBH_4$ concentrations) at different current densities. (f) Cycling stability at 3 A g^{-1} of pristine $ZnCo_2O_4$ and $ZnCo_2O_4$-0.5 nanoclusters. (g) Linear relationship of log(*i*) and log(*v*) for pristine $ZnCo_2O_4$ and $ZnCo_2O_4$-0.5 nanoclusters. (h) Separation of capacitance (red) controlled currents of $ZnCo_2O_4$-0.5 nanoclusters at 0.4 mV s^{-1}. (i) Contributions of capacitance-controlled (red region) and diffusion-controlled (blue region) processes at different scan rates of $ZnCo_2O_4$-0.5 nanoclusters.

$$ZnCo_2O_4 + H_2O + OH^- \leftrightarrow 2CoOOH + ZnOOH + e^- \quad (6)$$

$$CoOOH + OH^- \leftrightarrow CoO_2 + H_2O + e^- \quad (7)$$

The CV curve exhibited a single pair of redox peaks due to the synergistic effect exerted by the redox reactions of M–O and M–O–OH (where M represents Zn and Co ions) associated with OH^-.[53] Simultaneously, the reduction of $ZnCo_2O_4$ results in the appearance of a cathodic peak and the oxidation of both CoOOH and ZnOOH leads to an anodic peak, which aligns with the previous research conducted on the $ZnCo_2O_4$ materials.[38,54]

Additionally, compared with the pristine $ZnCo_2O_4$, the CV curve of $ZnCo_2O_4$-0.5 exhibits a larger integral area and higher peak current density due to the enhanced adsorption capacity of OH^- resulting from an increased number of oxygen vacancies on the material surface.[55] Evidently, the synergistic effect of oxygen vacancies and 3D nanostructures leads to an accelerated redox reaction rate and consequently, improved charge storage capability. Fig. 4b and S6a† present CV curves of the $ZnCo_2O_4$-0.5 and $ZnCo_2O_4$ at scan rates varying from 5 to 100 mV s^{-1} in a potential range of −0.4–0.6 V, respectively. With the increase in scan rate, a slight shift occurs in the position of both the anode and cathode peaks due to the rapid redox reaction at the electrode–electrolyte interface while the overall shape of the CV curve remained unaltered, representing the typical Faraday reaction and reversible redox reaction of the electrode material.[56]

The capacity optimization of $ZnCo_2O_4$ with the introduction of oxygen vacancies was further explored by galvanostatic charge–discharge (GCD) tests at 1 A g^{-1} within the potential range from 0 to 0.35 V presented in Fig. 4c. The discharge time of $ZnCo_2O_4$-0.5 is longer than that of others, indicating its superior electrochemical capacity. The calculated specific capacitance of $ZnCo_2O_4$-0.5 is 2685.7 F g^{-1} at 1 A g^{-1}, which significantly surpasses that of the $ZnCo_2O_4$ (1525.7 F g^{-1}). Moreover, as shown in Fig. 4d and S6b,† the GCD curves of $ZnCo_2O_4$-0.5 and $ZnCo_2O_4$ demonstrate a distinct voltage plateau accompanied by nonlinear and symmetrical characteristics, thereby providing additional substantiation for the

pseudo-capacitance behavior with excellent reversibility.[57] As summarized in Fig. 4e, the specific capacitance of the $ZnCo_2O_4$ samples after reduction treatment using different concentrations of $NaBH_4$ at different current densities was calculated from the GCD curves. The electrochemical performance of $ZnCo_2O_4$ samples treated with 0.5 M $NaBH_4$ was superior compared to other conditions. The specific capacitance of the $ZnCo_2O_4$-0.5 electrode is 2685.7, 2611.4, 2554.3, 2457.1, and 2200.2 F g^{-1} at 1, 2, 3, 5, and 10 A g^{-1}, respectively. The noteworthy observation is that the specific capacitance of the $ZnCo_2O_4$ is merely 1525.7, 1462.9, 1414.3, 1357.1, and 1257.1 F g^{-1} even under identical current densities. The rate capability of $ZnCo_2O_4$-0.5 is commendable, as it demonstrates a capacity retention of 83.7% even under an increased current density of 10 A g^{-1}. This superior electrochemical performance is attributed to the presence of richness-enabled oxygen vacancies on the surface, which can provide more active sites and lead to fast transmission of electrons and ions.[11] The CV curves of bare NF substrate and $ZnCo_2O_4$-0.5 at 50 mV s^{-1} are shown in Fig.S7a.† By incorporating the CV curves, the contribution of the NF substrate to the electrochemical reaction is considered negligible, as it accounts for only 1.07% of the ZCO-0.5 area. The GCD curves and specific capacitance of the NF substrate are also presented in Fig. S7b and S8,† respectively. The calculated specific capacitance of the NF substrate is 21.2 F g^{-1} at 1 A g^{-1}. The aforementioned results indicate that the contribution of NF substrate to the overall capacitance can be disregarded.

As shown in Fig. 4f, the cycling stability of the $ZnCo_2O_4$-0.5 and $ZnCo_2O_4$ electrodes was investigated by conducting repetitive galvanostatic charge–discharge tests within the voltage range of 0 to 0.35 V, at a high current density of 3 A g^{-1} for a total of 10 000 cycles, which serves as a crucial indicator for evaluating the commercial applications of supercapacitors. The specific capacitance of both $ZnCo_2O_4$ and $ZnCo_2O_4$-0.5 electrodes exhibited a marginal increase in the initial stage, which can be attributed to the ongoing activation process.[58] The cycling stability of $ZnCo_2O_4$ was found to be insufficient, with only 63.16% of the initial capacitance retained after 10 000 cycles. However, subsequent chemical reduction resulted in an improvement in cycling stability to 72.59%, indicating the enhanced cycling stability of $ZnCo_2O_4$-0.5 can be attributed to the introduction of oxygen vacancies. The excellent cycling stability of $ZnCo_2O_4$-0.5 electrode is ascribed to the reversible electrochemical reaction and robust mechanical stability. A comparison of the electrochemical performance with the reported $ZnCo_2O_4$ electrodes is shown in Table S3.†

The superior electrochemical performance of $ZnCo_2O_4$-0.5 is attributed to the following reasons:

(1) The oxygen vacancies can serve as active sites involved in the Faraday redox reaction, facilitating the adsorption of OH^- species onto the surface of $ZnCo_2O_4$-0.5 nanoclusters, thereby accelerating the kinetics of surface reactions and reducing the energy barrier.[59]

(2) The presence of oxygen vacancies facilitates the removal of oxygen atoms from Zn–O and Co–O bonds, leading to electron migration from the oxygen 2p orbitals towards Zn^{2+}, Co^{3+}, and O atoms, increasing the degree of electron delocalization. The enhancement in the quantity of free electrons significantly enhances the intrinsic electrical conductivity of the $ZnCo_2O_4$-0.5 nanoclusters.[46]

(3) The introduction of oxygen vacancies optimizes the electronic structure of $ZnCo_2O_4$-0.5. The upward shift of the valence band and the downward shift of the conduction band effectively reduce the path length for electron transport processes in the bandgap, thereby enhancing the electronic conductivity of $ZnCo_2O_4$-0.5 nanoclusters.[60]

(4) Oxygen vacancies can also act as shallow donors, enhancing the diffusion of charge carriers and optimizing the electrochemical performance of $ZnCo_2O_4$-0.5 nanoclusters.[61]

(5) The $ZnCo_2O_4$-0.5 nanoclusters exhibit a distinctive coral-like 3D hierarchical porous structure, comprising micropores and mesopores, thereby providing enhanced electroactive surface area and effectively mitigating volume changes during charge and discharge processes.[62] The NF substrate functions as a conductive grid, facilitating supplementary pathways for charge transfer.[63]

The intrinsic electrical properties of $ZnCo_2O_4$ and $ZnCo_2O_4$-0.5 electrodes were further investigated *via* electrochemical impedance spectroscopy (EIS) tests, in the frequency range of 100 kHz to 0.01 Hz. The EIS curves (Fig. S9†) exhibit distinct characteristics: the low-frequency region demonstrates a slope indicative of ion diffusion resistivity between the electrolyte and electrode,[64] and the high-frequency region displays a semi-circle, while the semi-circle diameter representing Faraday charge transfer resistance (R_{ct}).[65] Additionally, the intercept on the real axis indicates the inherent resistance of the electrochemical system (R_s), which encompasses the intrinsic resistance of the active material, ionic resistance of electrolyte, and contact resistance between current collector and active material.[66] The $ZnCo_2O_4$-0.5 exhibits a steeper slope in the low-frequency region compared to $ZnCo_2O_4$, implying an enhanced electron diffusion rate and reduced electrolyte diffusion resistance.[67] The fitting value of R_s decreased from 0.59 to 0.40 Ω, and R_{ct} decreased from 2.84 to 1.28 Ω after the introduction of oxygen vacancies. The EIS results imply that the introduction of oxygen vacancies enhances the original conductivity of pristine $ZnCo_2O_4$ electrode materials, while the 3D coral-like microstructure facilitates charge transfer and accelerates redox reaction kinetics.

To better investigate the impact of oxygen vacancies on the kinetic behavior and charge storage mechanism of $ZnCo_2O_4$-0.5, the mathematical relationship between the peak current (i) *versus* the scan rate (v), as obtained from the analysis of the CV curves under low current density, can be described by the following equation:[68]

$$i = av^b \tag{8}$$

$$\log i = b \log v + \log a \tag{9}$$

where a and b are fitting constants. Generally, when the value of b approaches 0.5 or 1, it indicates diffusion-controlled or capacitance-controlled behavior, respectively.[69] The slope of the fitting line in Fig. 4g is typically represented by the variable b,

which can be derived by plotting $\log(i)$ against $\log(v)$. The computed values of b for pristine $ZnCo_2O_4$ and $ZnCo_2O_4$-0.5 are 0.76 and 0.86, respectively, indicating that both samples are governed by diffusion/capacitance-controlled behavior.[70] Meanwhile, the b value of $ZnCo_2O_4$ is lower than that of $ZnCo_2O_4$-0.5, suggesting that the introduction of oxygen vacancies increased the number of active sites in the electrochemical reactions and expedites the redox reaction process of $ZnCo_2O_4$-0.5.[57] Furthermore, the contributions of diffusion-controlled and capacitance-controlled processes can be further quantified *via* the following equation:[71]

$$i = k_1 v + k_2 v^{1/2} \quad (10)$$

where k_1 and k_2 are constants, $k_1 v$ and $k_2 v^{1/2}$ represent the capacitance-controlled and diffusion-controlled behavior, respectively. Fig. 4h illustrates that the capacitance contribution to the overall capacity reaches 50.81% at a scan rate of 0.4 mV s^{-1}. As shown in Fig. 4i, when the scan rate is 0.2, 0.4, 0.6, 0.8, 1, and 2 mV s^{-1}, the capacitance contribution of the $ZnCo_2O_4$-0.5 electrode amounts to 50.81%, 64.17%, 74.49%, 77.1%, 84.28%, and 91.68%, respectively. In contrast, the $ZnCo_2O_4$ electrode exhibits lower capacitance contributions of only 43.12%, 56.07%, 64.43%, 59.25%, 75.83%, and 84.02% under the same current density conditions (Fig. S10†). The above results not only demonstrate that capacitance constitutes the dominant component of the total capacitance but also indicate that the introduction of oxygen vacancies increases the proportion of capacitance, corresponding to an increase in the value of b. The findings also reveal that the impact of diffusion processes plays a pivotal role in the entirety of the electrochemical phenomenon, particularly at low scan rates, suggesting that $ZnCo_2O_4$-0.5 facilitates the permeability of OH^- ions. As the scan rate elevates, the ability of the electrolyte ions to embed is constrained, allowing the capacitance to assume a dominant role.[72] The kinetic analysis investigates the synergistic effects of capacitance and diffusion contribution on enhancing the redox reaction of $ZnCo_2O_4$-0.5 materials.

To investigate the electrochemical performance of $ZnCo_2O_4$-0.5 in practical applications, the $ZnCo_2O_4$-0.5 nanoclusters//AC ASC device was fabricated with $ZnCo_2O_4$-0.5 nanoclusters as the positive electrode, AC as the negative electrode, and 6 M KOH as the electrolyte, respectively (Fig. 5a). When the scan rate is set to 5 mV s^{-1}, the CV curves of $ZnCo_2O_4$-0.5 and AC are illustrated in Fig. S11a.† Specifically, the shape of the CV curves represents the electrical double layer capacitance (EDLC) behavior of AC in the range of −1–0 V, while the obvious redox peaks of $ZnCo_2O_4$-0.5 in the range of 0–0.6 V indicate that the capacitance is derived from pseudo-capacitor behavior.[73] The utilization of distinct electrode materials for the positive and negative electrodes effectively expands the voltage range of the ASC device.[74] The CV curves of the $ZnCo_2O_4$-0.5 nanoclusters//AC ASC device obtained at different voltage windows are presented in Fig. S11b.† When the voltage is increased to 1.8 V, polarization effects during the charge and discharge process cause distortion in the CV curve, therefore, the optimal operating potential is 0–1.6 V.[15] The CV curves of the $ZnCo_2O_4$-0.5 nanoclusters//AC ASC device at different scan rates are shown in Fig. 5b, and the shape of CV curve is well retained as the scan rate increases. The well-defined voltage plateau and nearly symmetrical charge–discharge curves in Fig. 5c further indicate the exceptional electrochemical properties, which are following the CV analysis. As summarized in Fig. 5d, the specific capacitance of the $ZnCo_2O_4$-0.5 nanoclusters//AC ASC device at different current densities calculated from the GCD curves are 141.1, 108.1, 96.3, 85.3, and 70.0 F g^{-1} at 0.2, 0.5, 1.0, 1.5, and 2 A g^{-1} respectively.

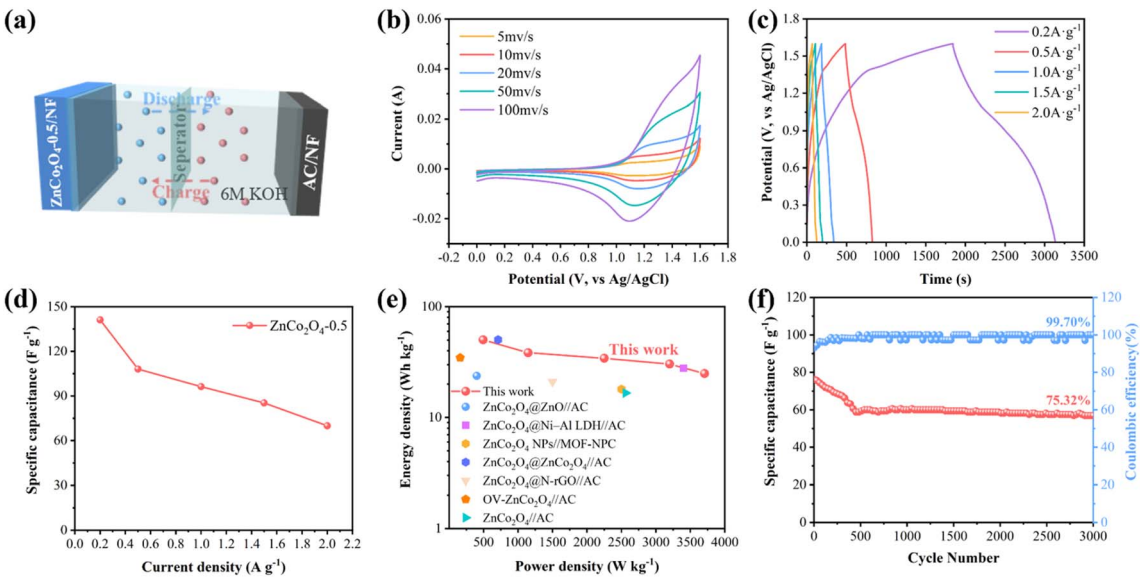

Fig. 5 Electrochemical performance of $ZnCo_2O_4$-0.5 nanoclusters//AC ASC device. (a) Schematic pattern of as-assembled ASC device. (b) CV curves at different scan rates. (c) GCD curves at different current densities. (d) Specific capacitance at different current densities. (e) Ragone plots of energy and power densities. (f) Cycling performance and coulombic efficiency after 3000 cycles at 2 A g^{-1}.

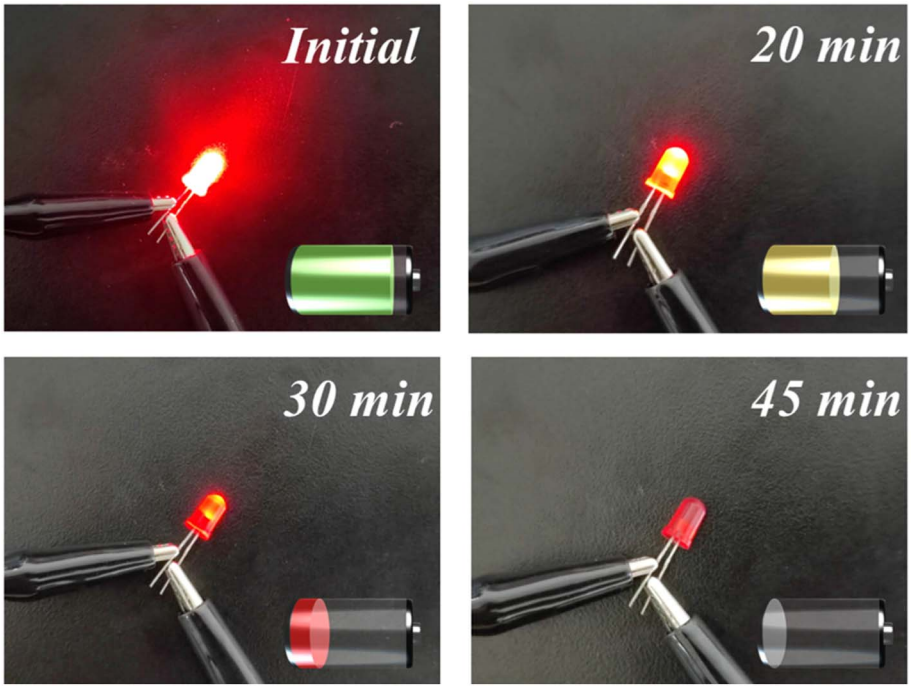

Fig. 6 The luminosity of the powering LED varies at different times.

In contrast, the specific capacitance of the $ZnCo_2O_4$ nanoclusters//AC ASC device is only 102.6 F g^{-1} at 0.2 A g^{-1}. The lifespan parameter plays a crucial role in the practical implementation. The long-term cycling stability of the $ZnCo_2O_4$-0.5 nanoclusters//AC device was also tested for 3000 continuous cycles at the constant current density of 2 A g^{-1}, which shows that the remarkable cycling performance with about 75.32% specific capacitance retention of its initial value after 3000 cycles and over as high as 99.70% coulombic efficiency retention (Fig. 5f). The initial stage may exhibit a weak capacity attenuation, which can be attributed to the insufficient adhesion of certain AC or $ZnCo_2O_4$-0.5 material on the NF substrate due to inherent imperfections in the coating process.[75] It's worth noting that energy density and power density are two crucial parameters for assessing the commercial application viability of ASC devices. As shown in Fig. 5e, the $ZnCo_2O_4$-0.5 nanoclusters//AC ASC device reaches a maximum energy density of 50.2 W h kg^{-1} at a power density of 493.7 W kg^{-1} and remains 24.9 W h kg^{-1} at 3705.9 W kg^{-1}, which is comparable to or approaching that most previously reported $ZnCo_2O_4$-based ASC device, such as $ZnCo_2O_4$@ZnO//AC (23.77 W h kg^{-1} at 399.98 W kg^{-1}),[76] $ZnCo_2O_4$@Ni-Al LDH//AC (27.84 W h kg^{-1} at 3400 W kg^{-1}),[77] $ZnCo_2O_4$ NPs//MOF-NPC (18 W h kg^{-1} at 2500 W kg^{-1}),[78] $ZnCo_2O_4$@$ZnCo_2O_4$//AC (50.41 W h kg^{-1} at 710.49 W kg^{-1}),[79] $ZnCo_2O_4$@N-rGO//AC (21 W h kg^{-1} at 1500 W kg^{-1}),[80] $ZnCo_2O_4$/$NiCo_2O_4$ @GO//AC (50.8 W h kg^{-1} at 800 W kg^{-1}),[81] OV-$ZnCo_2O_4$//AC (34.6 W h kg^{-1} at 160 W kg^{-1}),[82] $ZnCo_2O_4$//AC (16.63 W h kg^{-1} at 2561 W kg^{-1}),[83] thereby highlighting the optimization of electrochemical performance by oxygen vacancies introduction. Additionally, the practical application of ASC devices utilizing $ZnCo_2O_4$-0.5 nanoclusters as a positive electrode assembly was further investigated. As shown in Fig. 6 two coin batteries connected in series could illuminate a LED bulb (2 V, 20 mA) and sustain brightness for over 30 minutes.

4. Conclusion

In conclusion, the synthesis of $ZnCo_2O_4$ was achieved through a straightforward and efficient hydrothermal and calcination procedure. Furthermore, by investigating the optimal reduction concentration of $NaBH_4$, 3D coral-like $ZnCo_2O_4$-0.5 nanomaterials with abundant oxygen vacancies were synthesized while preserving the original morphology of $ZnCo_2O_4$. Compared to the $ZnCo_2O_4$ (1525.7 F g^{-1}), the specific capacitance of the $ZnCo_2O_4$-0.5 electrode achieves 2685.7 F g^{-1} at the current density of 1 A g^{-1}, exhibiting an outstanding rate capability (maintaining more than 83.71% of its capacitance at 10 A g^{-1}). The constructed $ZnCo_2O_4$-0.5 nanoclusters//AC ASC device delivers a maximum energy density of 50.2 W h kg^{-1} at the power density of 493.7 W kg^{-1}, demonstrating inspiring cycling stability. The findings robustly confirm that the strategic integration of oxygen vacancies in metal oxides constitutes a novel and efficient method to enhance electrochemical performance.

Author contributions

Yanlei Bi: conceptualization, methodology, formal analysis, writing – original draft. Huiqing Fan: conceptualization, project administration, funding acquisition, writing – review & editing. Chuansen Hu: methodology, formal analysis. Ru Wang:

methodology, formal analysis. Lujie Niu: writing – review & editing. Guangwu Wen: supervision. Lu-Chang Qin: supervision, validation, writing – review & editing.

Conflicts of interest

There are no conflicts to declare.

Acknowledgements

This work was financially supported by the Natural Science Foundation of Shandong Province (Grant No. ZR2019BB036).

References

1 X. Zou, C. Dong, Y. Jin, D. Wang, L. Li, S. Wu, Z. Xu, Y. Chen, Z. Li and H. Yang, *Colloids Surf., A*, 2023, **672**, 131715.
2 Y. Wang, X. Wu, Y. Han and T. Li, *J. Energy Storage*, 2021, **42**, 103053.
3 Y. Sun, Y. Jin, Z. Jiang and L. Li, *Eng. Failure Anal.*, 2023, **149**, 107259.
4 N. Roy, K. S. Kumar, B. D. P. Raju, A. M. Karami, G. R. Reddy, H. R. Barai and S. W. Joo, *Colloids Surf., A*, 2024, **685**, 133240.
5 F. Naseri, S. Karimi, E. Farjah and E. Schaltz, *Renewable Sustainable Energy Rev.*, 2022, **155**, 111913.
6 A. Joseph and T. Thomas, *Prog. Solid State Chem.*, 2022, **68**, 100381.
7 W. Guo, D.-F. Chai, J. Li, J. Lv, J. Wang, D. Guo, G. Sui and J. Xing, *J. Energy Storage*, 2022, **52**, 104849.
8 J. Li, W. Jiang and D. Wang, *Colloids Surf., A*, 2023, **658**, 130750.
9 T. Ramachandran and F. Hamed, *J. Phys. Chem. Solids*, 2024, **188**, 111915.
10 T. Ramachandran, F. Hamed, R. K. Raji, S. M. Majhi, D. Barik, Y. A. Kumar, R. M. Jauhar, M. P. Pachamuthu, L. Vijayalakshmi and S. Ansar, *J. Phys. Chem. Solids*, 2023, **180**, 111467.
11 Y. Feng, W. Liu, Y. Wang, W. Gao, J. Li, K. Liu, X. Wang and J. Jiang, *J. Power Sources*, 2020, **458**, 228005.
12 R. Jiang, S. Wang, M. Du, L. Zhang, J. Cao, Y. Zeng, M. Zhang and Y. Sui, *Colloids Surf., A*, 2023, **675**, 132042.
13 L. Yuan, Y. Liu, N. Xin and R. He, *J. Energy Storage*, 2022, **52**, 104727.
14 T. Ramachandran, F. Hamed, Y. A. Kumar, R. K. Raji and H. H. Hegazy, *J. Energy Storage*, 2023, **73**, 109299.
15 S. Li, H. Fan, Y. Yang, Y. Bi, G. Wen and L.-C. Qin, *J. Alloys Compd.*, 2022, **920**, 165861.
16 J. Bhagwan, S. Khaja Hussain and J. S. Yu, *J. Alloys Compd.*, 2020, **815**, 152456.
17 M. Isacfranklin, S. Daphine, R. Yuvakkumar, L. Kungumadevi, G. Ravi, A. G. Al-Sehemi and D. Velauthapillai, *Ceram. Int.*, 2022, **48**, 24745–24750.
18 Y. Bai, Y. Ma, S. Zheng, C. Zhang, C. Hu, B. Liang, Y. Xu, G. Huang and R. Yang, *Colloids Surf., A*, 2022, **647**, 129064.
19 S. Meena, K. S. Anantharaju, S. Malini, A. Dey, L. Renuka, S. C. Prashantha and Y. S. Vidya, *Ceram. Int.*, 2021, **47**, 14723–14740.
20 Y. Wu, Y. Wang, P. Zhu, X. Ye, R. Liu and W. Cai, *Appl. Surf. Sci.*, 2022, **606**, 154863.
21 Z. Xu, J. Jiang, M. Wang, J. Wang, Y. Tang, S. Li and J. Liu, *Sep. Purif. Technol.*, 2023, **304**, 122055.
22 R. Liu, J. Feng, R. Tang and T. Meng, *Chem. Eng. J.*, 2023, **468**, 143766.
23 Y. Wang, X. Xiao, Q. Li and H. Pang, *Small*, 2018, **14**, e1802193.
24 J. Yuan, W. Feng, Y. Zhang, J. Xiao, X. Zhang, Y. Wu, W. Ni, H. Huang and W. Dai, *Adv. Mater.*, 2024, **36**, e2303845.
25 Y. Liu, Z. Ma, N. Xin, Y. Ying and W. Shi, *J. Colloid Interface Sci.*, 2021, **601**, 793–802.
26 X. Zhang, X. Liu, Y. Zeng, Y. Tong and X. Lu, *Small Methods*, 2020, **4**, 190823.
27 S. Khaja Hussain and J. H. Bang, *Phys. Chem. Chem. Phys.*, 2023, **25**, 11892–11907.
28 Q. Song, S. Zhou, S. Wang, S. Li, L. Xu and J. Qiu, *Chem. Eng. J.*, 2023, **461**, 142033.
29 L. Fu, S. Zhou, M. Xiang, J. Yang, W. Fan, Z. Yang and J. Ou, *J. Electroanal. Chem.*, 2022, **921**, 116650.
30 G. Zhuang, Y. Chen, Z. Zhuang, Y. Yu and J. Yu, *Sci. China Mater.*, 2020, **63**, 2089–2118.
31 J. Kumar, H. J. Jung, R. R. Neiber, R. A. Soomro, Y. J. Kwon, N. U. Hassan, M. Shon, J. H. Lee, K. Y. Baek and K. Y. Cho, *Int. J. Energy Res.*, 2022, **46**, 7055–7081.
32 X. Wei, C. Chen, X. Z. Fu and S. Wang, *Adv. Energy Mater.*, 2023, **14**, 2303027.
33 H. Fan, H. Di, Y. Bi, R. Wang, G. Wen and L. C. Qin, *RSC Adv.*, 2024, **14**, 650–661.
34 J. Yue, G. Lu, P. Zhang, Y. Wu, Z. Cheng and X. Kang, *Colloids Surf., A*, 2019, **569**, 10–17.
35 A. Zhang, R. Gao, L. Hu, X. Zang, R. Yang, S. Wang, S. Yao, Z. Yang and H. Hao, *Chem. Eng. J.*, 2021, **417**, 129186.
36 Q. Ma, F. Cui, J. Zhang, X. Qi and T. Cui, *Appl. Surf. Sci.*, 2022, **578**, 152001.
37 B. Chettiannan, S. Mathan, G. Arumugam, A. Srinivasan and R. Rajendran, *J. Energy Storage*, 2024, **77**, 110008.
38 B. Naresh, C. Kuchi, S. K. Kummara, O. R. Ankinapalli and P. S. Reddy, *Synth. Met.*, 2023, **293**, 117283.
39 X. Li, M. Zhang, L. Wu, Q. Fu and H. Gao, *J. Alloys Compd.*, 2019, **773**, 367–375.
40 G. M. Tomboc, H. S. Jadhav and H. Kim, *Chem. Eng. J.*, 2017, **308**, 202–213.
41 M. Yuan, Z. Sun, Z. Wu, D. Wang, H. Yang, C. Nan, H. Li, W. Zhang and G. Sun, *J. Colloid Interface Sci.*, 2022, **608**, 1384–1392.
42 D. A. Alshammari, I. A. Ahmed, S. D. Alahmari, M. Abdullah, S. Aman, N. Ahmad, A. M. A. Henaish, Z. Ahmad, H. M. T. Farid and Z. M. El-Bahy, *J. Energy Storage*, 2024, **75**, 109886.
43 C. Zhang, L. Lu, S. Hao, S. Fang, Q. Sui, J. Li, Y. Zou, F. Xu, L. Sun, C. Xiang and J. Xie, *J. Energy Storage*, 2024, **77**, 109983.
44 Z. Wu, X. Hu, C. Cai, Y. Wang, X. Li, J. Wen, B. Li and H. Gong, *J. Colloid Interface Sci.*, 2024, **657**, 75–82.
45 C. Wang, G. Sui, D. Guo, J. Li, Y. Zhuang, W. Guo, Y. Zhou, X. Yang and D.-F. Chai, *J. Energy Storage*, 2022, **49**, 104083.

46 D. Yan, W. Wang, X. Luo, C. Chen, Y. Zeng and Z. Zhu, *Chem. Eng. J.*, 2018, **334**, 864–872.
47 P. Suggana, E. P. Kumar, K. Chandrasekhar Reddy, M. V. Lakshmaiah, S. W. Joo and G. R. Reddy, *Colloids Surf., A*, 2023, **669**, 131423.
48 D. Cai, Q. Cao, J. Du, Y. Liu, F. Bu, Y. Yan, X. Lu, Q. Xia, D. Zhou and Y. Xia, *Batteries Supercaps*, 2021, **5**, 1–11.
49 Y. Zheng, H. Che, A. Liu, X. Liu, T. Tian, Z. Guo, J. Mu, X. Zhang, Y. Wang and Z. Zhang, *Colloids Surf., A*, 2023, **675**, 132029.
50 J. Xu, Z. Meng, Z. Hao, X. Sun, H. Nan, H. Liu, Y. Wang, W. Shi, H. Tian and X. Hu, *J. Colloid Interface Sci.*, 2022, **609**, 878–889.
51 H. Yu, H. Zhao, Y. Wu, B. Chen and J. Sun, *J. Phys. Chem. Solids*, 2020, **140**, 109385.
52 Y. Shang, T. Xie, Y. Gai, L. Su, L. Gong, H. Lv and F. Dong, *Electrochim. Acta*, 2017, **253**, 281–290.
53 G. R. Reddy, G. R. Dillip, T. V. M. Sreekanth, R. Rajavaram, B. D. P. Raju, P. C. Nagajyothi and J. Shim, *Appl. Surf. Sci.*, 2020, **529**, 147123.
54 A. J. C. Mary and A. C. Bose, *Appl. Surf. Sci.*, 2018, **449**, 105–112.
55 X. Xu, H. Lu, D. Xu, P. Zhou, Y. Ying, L. Li and Y. Liu, *Appl. Surf. Sci.*, 2023, **614**, 156174.
56 B. Zhang, L. Gao, H. Bai, Y. Li, B. Jia, X. Zhou, A. Li and L. Li, *J. Alloys Compd.*, 2023, **934**, 167979.
57 J. Ye, X. Zhai, L. Chen, W. Guo, T. Gu, Y. Shi, J. Hou, F. Han, Y. Liu, C. Fan, G. Wang, S. Peng and X. Guo, *J. Energy Chem.*, 2021, **62**, 252–261.
58 S. Chen, Q. Yang, J. Shi, Y. Ying and Y. Liu, *Colloids Surf., A*, 2022, **635**, 128078.
59 J. Zhao, G. Lu, Y. Wu, P. Zhang, J. Yue, Z. Cheng, J. Zhang and X. Kang, *Colloids Surf., A*, 2020, **603**, 125254.
60 D. Zu, H. Wang, S. Lin, G. Ou, H. Wei, S. Sun and H. Wu, *Nano Res.*, 2019, **12**, 2150–2163.
61 R. Wei, Y. Lu and Y. Xu, *Sci. China: Chem.*, 2021, **64**, 1826–1853.
62 Y. Li, J. Mei, L. Wu, Q. Xu and Z. Li, *Int. J. Hydrogen Energy*, 2024, **49**, 67–80.
63 K. Krishnamoorthy, G. K. Veerasubramani, S. Radhakrishnan and S. J. Kim, *Chem. Eng. J.*, 2014, **251**, 116–122.
64 M. Xu, M. Sun, S. u. Rehman, K. Ge, X. Hu, H. Ding, J. Liu and H. Bi, *Chin. Chem. Lett.*, 2021, **32**, 2027–2032.
65 J. Wang, Y. Luo, T. Xu, Z. Guo, G. Chen, Y. Ren, Y. Xue, N. Cai, H. Li and F. Yu, *J. Ind. Eng. Chem.*, 2023, **118**, 70–77.
66 X. Fu, Z. Zhang, Y. Zheng, J. Lu, S. Cheng, J. Su, H. Wei and Y. Gao, *J. Colloid Interface Sci.*, 2024, **653**, 1272–1282.
67 C. Ryu, H. M. Do and J. B. In, *Appl. Surf. Sci.*, 2024, **643**, 158696.
68 H. Wang, N. Mi, S. Sun, W. Zhang and S. Yao, *J. Alloys Compd.*, 2021, **869**, 159294.
69 P. Qi, H. Wang, Y. Lu, M. Chen, G. Liu, W. Li, C. Huang and Y. Tang, *J. Alloys Compd.*, 2022, **895**, 162535.
70 J. Sun, Y. Wang, J. Zhou, K. Chen, K. Tao, W. Zhao and L. Han, *Inorg. Chem.*, 2022, **61**, 4283–4291.
71 S. Xiong, X. Lin, S. Liu, S. Weng, S. Jiang, Y. Jiao, Y. Xu and J. Cheng, *Vacuum*, 2020, **182**, 109692.
72 X. Wei, X. Zhou, L. Li, W. Feng and H. Wu, *Appl. Surf. Sci.*, 2023, **613**, 155959.
73 S. Wei, C. Wan, L. Zhang, X. Liu, W. Tian, J. Su, W. Cheng and Y. Wu, *Chem. Eng. J.*, 2022, **429**, 132242.
74 T. Ramachandran, S. S. Sana, K. D. Kumar, Y. A. Kumar, H. H. Hegazy and S. C. Kim, *J. Energy Storage*, 2023, **73**, 109096.
75 J. Li, R. Lian, J. Wang, S. He, S. P. Jiang and Z. Rui, *Electrochim. Acta*, 2020, **331**, 135395.
76 Q. Ma, F. Cui, J. Zhang and T. Cui, *J. Colloid Interface Sci.*, 2023, **629**, 649–659.
77 X. Bai, D. Cao and H. Zhang, *Ceram. Int.*, 2019, **45**, 14943–14952.
78 D. He, Y. Gao, Y. Yao, L. Wu, J. Zhang, Z. H. Huang and M. X. Wang, *Front. Chem.*, 2020, **8**, 719.
79 P. Sivakumar, L. Kulandaivel, J. Park, C. J. Raj, R. Manikandan and H. Jung, *J. Alloys Compd.*, 2023, **952**, 170042.
80 G. Vignesh, R. Ranjithkumar, P. Devendran, N. Nallamuthu, S. Sudhahar and M. Krishna Kumar, *Mater. Sci. Eng., B*, 2023, **290**, 116328.
81 X. Chen, N. Xin, Y. Li, C. Sun, L. Li, Y. Ying, W. Shi and Y. Liu, *J. Mater. Sci. Technol.*, 2022, **127**, 236–244.
82 K. Xiang, D. Wu, Y. Fan, W. You and D. Zhang, *Chem. Eng. J.*, 2021, **425**, 130583.
83 B. Guan, D. Guo, L. Hu, G. Zhang, T. Fu, W. Ren, J. Li and Q. Li, *J. Mater. Chem. A*, 2014, **2**, 16116–16123.